Subwavelength spatially resolved coordination chemistry of metal-organic framework glass blends

Sean M. Collins,[*,†] Demie M. Kepaptsoglou,[‡,§] Keith T. Butler,[⊥] Louis Longley,[†] Thomas D. Bennett,[†] Quentin M. Ramasse,[‡,∥] and Paul A. Midgley[†]

[†]Department of Materials Science and Metallurgy, University of Cambridge, 27 Charles Babbage Road, Cambridge CB3 0FS, United Kingdom

[‡]SuperSTEM Laboratory, SciTech Daresbury Campus, Daresbury WA4 4AD, United Kingdom

[§]Department of Physics, University of York, Heslington, York YO10 5DD, United Kingdom

[⊥]ISIS Facility, Rutherford Appleton Laboratory, Harwell Oxford, Didcot OX11 0QX, United Kingdom

[∥]School of Chemical and Process Engineering and School of Physics, University of Leeds, Leeds LS2 9JT, United Kingdom

Supporting Information Placeholder

ABSTRACT: Microstructured metal-organic framework (MOF) glasses have been produced by combining two amorphous MOFs. However, the electronic structure of these materials has not been interrogated at the length scales of the chemical domains formed in these glasses. Here, we report a subwavelength spatially resolved physicochemical analysis of the electronic states at visible and UV energies in a blend of two zeolitic imidazolate frameworks (ZIFs), ZIF-4-Co and ZIF-62-Zn. By combining spectroscopy at visible and UV energies as well as at core ionization energies in electron energy loss spectroscopy in the scanning transmission electron microscope (STEM-EELS) with density functional theory calculations, we show that domains less than 200 nm in size retain the electronic structure of the precursor crystalline ZIF phases. Prototypical signatures of coordination chemistry including *d-d* transitions in ZIF-4-Co are assigned and mapped with nanoscale precision.

The coordination chemistry between ligands and metal centers underpins the structure and reactivity of metal-organic frameworks (MOFs). The diversity of bond strengths and structures possible in the coordination environment gives rise to important properties of MOFs such as tunable porosity for gas storage,[1] adjustable activity of binding sites for gas separations[2] and catalysis,[3] and controlled optical properties in photocatalysis[4] and sensing.[5] Recently, the exploration of amorphous MOFs that retain the critical coordination chemistry has launched research into improved processability, hazardous waste trapping, and melt-quenched glasses with distinct mechanical properties.[6–8] Amorphous materials have typically been described statistically, using ensemble structural and spectroscopic techniques, but these approaches miss microscopic heterogeneity and require alternatives for nanometer-scale assessment of electronic structure variation.

Here, we present spatially resolved spectroscopy of a zeolitic imidazolate framework (ZIF) glass blend[9] at visible to X-ray photon energies using electron energy loss spectroscopy (EELS) in scanning transmission electron microscopy (STEM). Spectroscopic characterization across multiple energy windows, with co-registered spatial maps, enables the detailed interpretation of the optical states at visible and UV energies of a blend of ZIF-4-Co $[Co(C_3H_3N_2)_2]$ and ZIF-62-Zn $[Zn(C_3H_3N_2)_{1.75}(C_7H_5N_2)_{0.25}]$. Co-based ZIFs show unique optical properties in ligand-metal as well as metal *d*-orbital transitions and provide a key signature of the geometry of the coordination environment.[4,10,11] Tetrahedral Co generally exhibits spin-allowed *d-d* transitions, in contrast to Laporte-forbidden transitions in octahedral coordination, and the electronic structure and underlying coordination of metal centers in blended melt-quenched MOF glasses represents a key, fundamental question so far only indirectly addressed by ensemble measurements.

The STEM-EELS technique consists of a focused nanometer to sub-nanometer electron beam that is rastered across a thin specimen. Electrons transmitted through the specimen have a probability of inelastic scattering which is determined by the quantum mechanical states of the specimen material, resulting in an energy loss spectrum. The intrinsic spread of the incident electron beam imposes a low-energy cut-off on accessible energies, but with monochromated electron microscopes spectroscopy from below 1 eV is routinely possible.[12,13] STEM-EELS has seen widespread application in the study of plasmonic nanoparticles due to the subwavelength characterization of optical properties the technique provides.[14–16] However, in only a few cases has STEM-EELS been applied to single-electron transitions due to their lower scattering cross-sections. STEM-EELS has been used previously to study excitons in $MoS_2/MoSe_2$[17] and intramolecular transitions in organic solar cell materials.[18–20] Non-dipole *d-d* transitions have also been observed by momentum-resolved STEM-EELS in more electron radiation resistant inorganic materials.[21]

Here, STEM-EELS of optically allowed *d-d* transitions is used as a direct probe of the coordination environment within a non-crystalline microstructured MOF glass blend. Combined with EELS at characteristic ionization edges (Co L_{23}, Zn L_{23}, C *K*, N *K*) and density functional theory (DFT) calculations, we show with deeply subwavelength spatial resolution that the electronic structure of ZIF-4-Co and ZIF-62-Zn are each preserved in the glass phase with clear evidence of Co *d-d* transitions in ZIF-4-Co domains as well as intra-ligand and ligand-metal transitions in ZIF-4-Co and ZIF-62-Zn glass domains below 200 nm in extent.

A blend of ZIF-4-Co and ZIF-62-Zn, hereby referred to as $(ZIF\text{-}4\text{-}Co)_{0.5}(ZIF\text{-}62\text{-}Zn)_{0.5}$, as reported in Ref. 9, was used for this work. Briefly, crystalline powders of ZIF-4-Co and ZIF-62-Zn were synthesized,[22,23] then mixed and heated to a temperature where the ZIF-62-Zn is liquid and the ZIF-4-Co is amorphous, and finally quenched to the solid state. The structure of liquid phase ZIFs consists of ligand-coordinated Zn^{2+} with sub-picosecond linker exchange in the liquid.[24] Details of the experimental parameters are described in the Supporting Information (SI). Spectrum images, consisting of EEL spectra recorded at each beam position, were acquired sequentially to cover energies in the UV-Vis (1-10 eV), bulk plasma (1-50 eV), C and N *K* (200-500 eV), and Co and Zn L_{23} (750-1200 eV) windows.

Figure 1(a) presents models of the ligands and coordination at metal centers in ZIF-4-Co and in ZIF-62-Zn. In ZIF-4-Co, tetrahedral positions are bridged by N-M coordination (M = metal) with imidazolate (Im, $C_3H_3N_2^-$) ligands,[22] giving the composition $Co(Im)_2$. In ZIF-62-Zn, the Zn^{2+} center is likewise N-M coordinated but with one position in every other Zn^{2+} bridged by a benzimidazolate ligand (bIm, $C_7H_5N_2^-$), giving the composition $Zn(Im)_{1.75}(bIm)_{0.25}$.[22] Consequently, in addition to differences in *d*-band filling, the bIm ligand is associated only with the ZIF-62-Zn precursor.

Isolated crystalline precursors were examined by EELS as a reference for the glass blend. Figure 1(b) presents spectra at 80 kV averaged over entire single-phase particles of ZIF-4-Co and ZIF-62-Zn. Figure 1(c) presents spectra at 300 kV extracted from selected areas of a particle of $(ZIF\text{-}4\text{-}Co)_{0.5}(ZIF\text{-}62\text{-}Zn)_{0.5}$ corresponding to Co-rich and Zn-rich regions. The inset shows an annular dark field (ADF) STEM micrograph showing mass-thickness contrast for reference. No domain structure was visible in ADF-STEM. EEL spectra were background subtracted to remove the contributions of electrons undergoing no energy loss, the zero loss peak (ZLP), and its continuum tail. Spectra in the blend reproduced the same spectral signals for the Co^{2+} and Zn^{2+} phases, respectively, with no dependence on incident beam energy (see also Fig. S1). In ZIF-4-Co and in the Co-rich domains of $(ZIF\text{-}4\text{-}Co)_{0.5}(ZIF\text{-}62\text{-}Zn)_{0.5}$, a rise in the EELS signal at 2 eV was observed followed by a gradual increase in the region of 4 eV and two peaks at 6 eV and 8 eV. In ZIF-62-Zn and in the Zn-rich domains of $(ZIF\text{-}4\text{-}Co)_{0.5}(ZIF\text{-}62\text{-}Zn)_{0.5}$, the first peak was observed at 4 eV followed by peaks at 5.8 eV and 7.5 eV. The relative intensities of the EELS signals were also distinct between Co^{2+} and Zn^{2+} domains.

These spectral signatures were in turn mapped to reveal the Co^{2+} and Zn^{2+} domain microstructure using a machine learning algorithm, non-negative matrix factorization (NMF), used successfully in low-loss EELS of plasmonic particles.[14,15] NMF performs particularly well in noisy data-sets with unknown peak shapes where peak fitting is challenging, as is the case using conditions to limit the electron dose. NMF separates the hyperspectral data-set obtained in STEM-EELS into a set of two-dimensional maps and corresponding spectral signatures. The non-negativity constraint is often sufficient to separate data consisting of a small number of spectral signatures that are distinct spectrally and spatially,[15] as is the case for the glass blend. Due to the weak constraint, NMF results are necessarily scrutinized as they are not guaranteed to be physical.

Figure 2(a)-(b) presents the NMF map and corresponding spectral signatures for the Co^{2+} and Zn^{2+} domains in the same particle as shown in Fig. 1(c). The peaks observed in selected area spectra (Fig. 1(c)) are reproduced in the NMF spectral factors in Fig. 2(b), confirming the separation arises from physical signals. Figure 2(c)-(e) shows the corresponding elemental EELS map, analyzed by independent component analysis (ICA).[25] The red regions correspond to the Co L_{23} signal and the blue regions correspond to

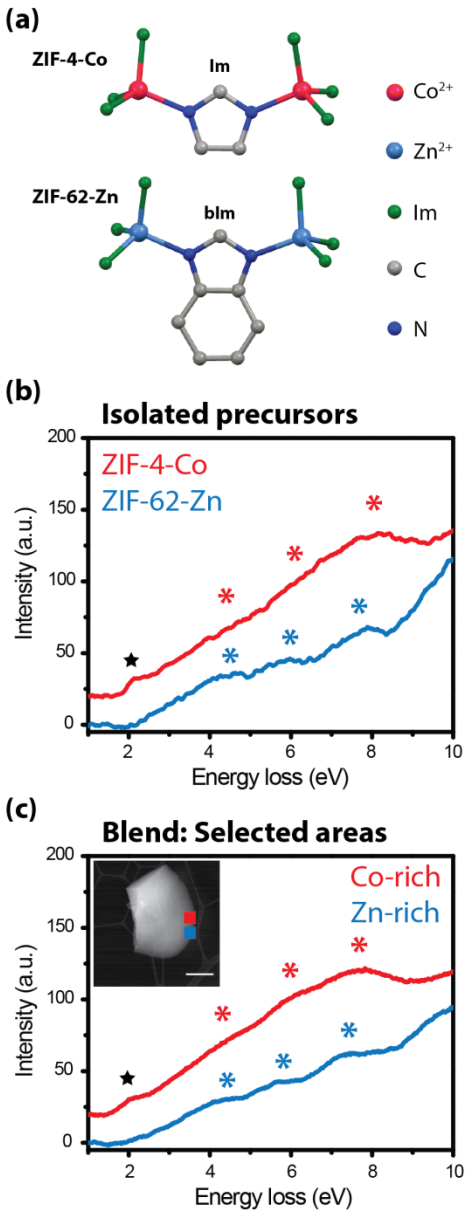

Figure 1. (a) Models of the local coordination involving the imidazolate (Im) ligand in ZIF-4-Co and the benzimidazolate (bIm) ligand in ZIF-62-Zn. (b) STEM-EELS spectra from single-phase ZIF-4-Co and ZIF-62-Zn precursor particles. (c) Selected area STEM-EELS spectra from a glass blend particle with the spatial locations marked on the inset ADF-STEM micrograph. The inset scale bar is 1 μm.

the Zn L_{23} signal. The maps in Fig. 2(a),(c) show identical distributions of the low energy and elemental signatures, revealing that the signatures at visible and UV energies arise from the Co^{2+} and Zn^{2+} domains. NMF maps of additional particles are shown in Fig. S2-S3. It should be noted that NMF picks up particularly on spectral differences, so the maps in Fig. 2(a) have some intensity overlap due to similarity in the spectral background between the Co^{2+} and Zn^{2+} domains. At the signal-to-noise ratio possible without significantly altering the MOF glass blend with the electron beam, it is unlikely that subtle changes at the interface itself are detectable (e.g., small amplitude or energy shifts due to conformational fluctuations or disorder). The mapping, however, demonstrates that the low energy EELS signals can be used to measure

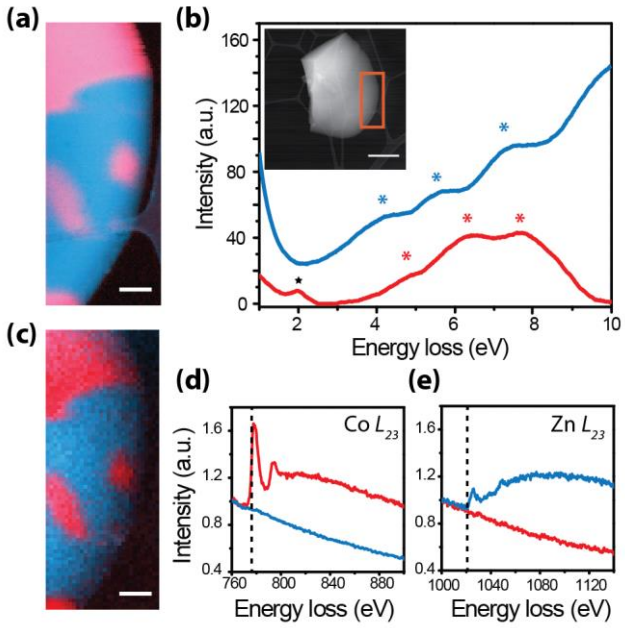

Figure 2. (a) STEM-EELS map and (b) corresponding spectral components for a $(ZIF\text{-}4\text{-}Co)_{0.5}(ZIF\text{-}62\text{-}Zn)_{0.5}$ glass blend particle obtained by non-negative matrix factorization. The inset ADF-STEM micrograph shows the region of the particle used for mapping. (c) STEM-EELS Elemental map and (d)-(e) corresponding spectra at the characteristic L_{23} ionization edges for Co and Zn obtained by independent component analysis. The dashed lines indicate the onset for the EELS edges. The scale bars are 150 nm. The inset scale bar is 1 μm.

the shape of domains with deep subwavelength spatial resolution, measured here at <15 nm across the interface (80% criterion). The abruptness of the interfaces in the NMF map likewise indicates that the electronic structure changes locally with the largely phase-segregated metal centers.

Figure 3 presents spectra obtained at 60 kV from a particle analyzed with a Hermes STEM (Nion) with superior energy resolution. The feature at 2-2.5 eV is visible as an abrupt onset in the spectrum from the Co^{2+} phase only. A peak at ~600 nm or 2 eV is a hallmark of tetrahedral Co in organometallic,[10,11] MOF,[4] and oxide materials.[26,27] Based on studies of single phase materials using ensemble spectroscopies, the EELS feature at 2-2.5 eV was therefore assigned as the $[^4A_2(F)\text{–}^4T_1(P)]$ *d-d* ligand field transition in ZIF-4-Co. Previous reports indicate that higher energy transitions may be expected to arise from ligand-metal transitions and intra-ligand transitions.[4]

DFT calculations were carried out to assign these transitions and to corroborate the experimental data. DFT calculations were carried out in VASP[28] on the crystalline phases of ZIF-4-Co and ZIF-62-Zn (see SI) due to the prohibitive size of amorphous network unit cells and given the close correspondence between experimental crystalline precursor and glass phases (Fig. 1). Figure 4 presents calculated loss functions, corresponding to the EEL spectrum (see also SI), and transition dipoles for ZIF-4-Co and ZIF-62-Zn. As in the experimental data, an onset in the loss function for ZIF-4-Co was observed at 2-2.5 eV followed by peaks at 6 and 8 eV. Likewise, the calculated loss function for ZIF-62-Zn exhibited a first peak at 4 eV followed by series of overlapping features at 5-8 eV. By inspection of the contributions to the transition in the absorption spectrum (Fig. 4(b)-(c) and Fig. S6), the peaks at 2-2.5 eV were assigned to Co *d-d* transitions. The strongest transitions in ZIF-4-Co at higher energy corresponded to Co *d*

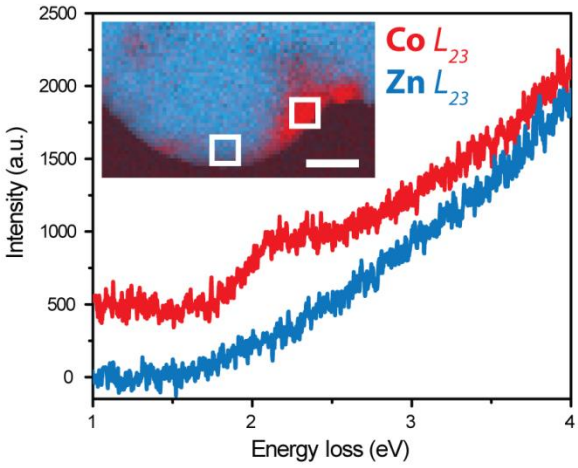

Figure 3. High resolution monochromated STEM-EELS selected area spectra. The inset shows the elemental map with white boxes indicating the locations of the selected areas. The scale bar is 250 nm. The spectra prior to background subtraction are shown in Fig. S4.

to ligand transitions at 4.8 and 5.5 eV. In ZIF-62-Zn, the lowest energy transition was assigned to an intra-ligand bIm transition at 4 eV followed by transitions at approximately 6 eV from N *p* states to delocalized Im states.

Additional absorption spectra and partial density of states calculations compared with experimental spectra including the bulk plasma frequency and the C *K* and N *K* ionization edges (Fig. S5-S8) provided further corroboration of the DFT calculations and evidence that the experimental glass blend did not exhibit significant electron beam induced damage. The DFT assignments identify key differences due to the ligand coordination in ZIF-4-Co and ZIF-62-Zn, providing strong, direct evidence of the retention of local tetrahedral coordination of the metal center in ZIF glasses. The Co *d* to ligand transition at UV energies further points to significant charge transfer in ZIF-4-Co domains in the glass blend, presenting opportunities for exploiting photocatalytic or sensing applications in a hybrid glass.

This development of the STEM-EELS technique invites the examination of the solid-liquid phase transition and the effect of quenching rates when such experiments become feasible (see also SI). The key results also highlight that the electronic structure of the precursor phases is retained in ZIF glass blends, indicating the distinct mechanical properties observed in glass blends[9] arise from interactions between domains in the glass. Due to the subwavelength scale of the optically distinct domains, the macroscopic optical properties of the blend will not be a simple summation of optical properties due to lensing and interference effects, presenting opportunities for engineering MOF glasses for dielectric optical applications. These findings prompt further study of coordination chemistry by STEM-EELS and exploration of optically active microstructured MOF glasses.

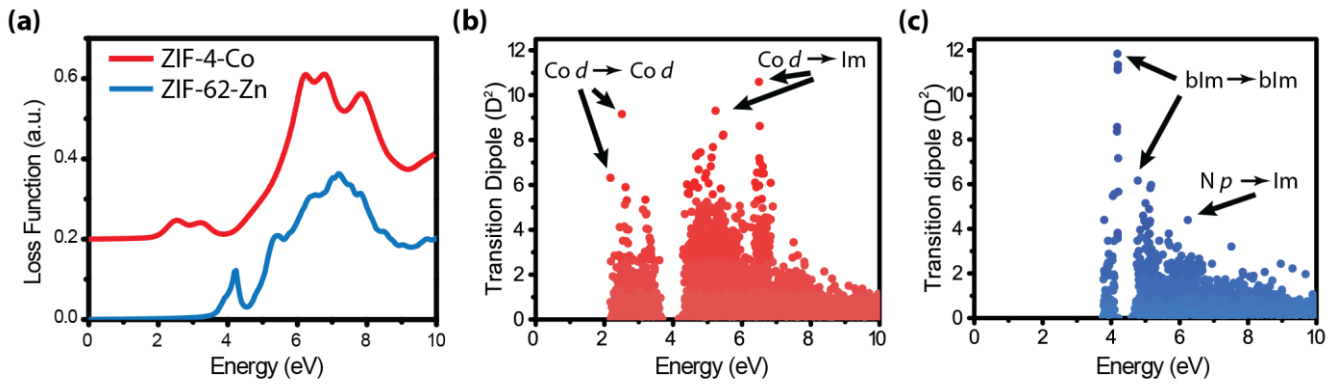

Figure 4. (a) Loss spectra for ZIF-4-Co and ZIF-62-Zn calculated by DFT. (b)-(c) Transition dipole oscillator strengths calculated and assigned according to orbital contributions for the excitations underlying the peaks in the loss function.

ASSOCIATED CONTENT

Supporting Information

Additional information on methods, dipole and non-dipole scattering in EELS, the loss function, prospects for *in situ* experiments, and additional figures related to experimental and calculated EELS and absorption spectra (PDF).

The Supporting Information is available free of charge on the ACS Publications website.

AUTHOR INFORMATION

Corresponding Author

*smc204@cam.ac.uk

Notes

The authors declare no competing financial interests.

ACKNOWLEDGMENT

S.M.C. acknowledges support from the Henslow Research Fellowship at Girton College, Cambridge. T.D.B. would like to thank the Royal Society for a University Research Fellowship (UF150021), and L.L. acknowledges an Engineering and Physical Sciences Research Council (EPSRC) studentship. P.A.M. thanks the EPSRC for financial support under grant number EP/R025517/1. SuperSTEM is the U.K. National Research Facility for Advanced Electron Microscopy, supported by the EPSRC. The research leading to these results has received funding from the European Research Council under the European Union's Seventh Framework Programme (FP7/2007-2013)/ERC grant agreement 291522-3DIMAGE.

REFERENCES

(1) Mason, J. A.; Oktawiec, J.; Taylor, M. K.; Hudson, M. R.; Rodriguez, J.; Bachman, J. E.; Gonzalez, M. I.; Cervellino, A.; Guagliardi, A.; Brown, C. M.; Llewellyn, P.L.; Masciocchi, N.; Long, J.R. Methane Storage in Flexible Metal–Organic Frameworks with Intrinsic Thermal Management. *Nature* **2015**, *527* (7578), 357–361.

(2) Bae, T.-H.; Lee, J. S.; Qiu, W.; Koros, W. J.; Jones, C. W.; Nair, S. A High-Performance Gas-Separation Membrane Containing Submicrometer-Sized Metal–Organic Framework Crystals. *Angew. Chem. 122* (51), 10059–10062.

(3) Mondloch, J. E.; Katz, M. J.; Isley Iii, W. C.; Ghosh, P.; Liao, P.; Bury, W.; Wagner, G. W.; Hall, M. G.; DeCoste, J. B.; Peterson, G. W.; Snurr, R.Q.; Cramer, C.J.; Hupp, J.T.; Farha, O.K Destruction of Chemical Warfare Agents Using Metal–Organic Frameworks. *Nat. Mater.* **2015**, *14* (5), 512–516.

(4) Pattengale, B.; Yang, S.; Ludwig, J.; Huang, Z.; Zhang, X.; Huang, J. Exceptionally Long-Lived Charge Separated State in Zeolitic Imidazolate Framework: Implication for Photocatalytic Applications. *J. Am. Chem. Soc.* **2016**, *138* (26), 8072–8075.

(5) Müller, P.; Wisser, F. M.; Freund, P.; Bon, V.; Senkovska, I.; Kaskel, S. Optical Sensors Using Solvatochromic Metal–Organic Frameworks. *Inorg. Chem.* **2017**, *56* (22), 14164–14169.

(6) Bennett, T. D.; Horike, S. Liquid, Glass and Amorphous Solid States of Coordination Polymers and Metal–Organic Frameworks. *Nat. Rev. Mater.* **2018**, *3*, 431–440.

(7) Bennett, T. D.; Yue, Y.; Li, P.; Qiao, A.; Tao, H.; Greaves, N. G.; Richards, T.; Lampronti, G. I.; Redfern, S. A. T.; Blanc, F.; Farha, O.K.; Hupp, J.T.; Cheetham, A.K.; Keen, D.A. Melt-Quenched Glasses of Metal–Organic Frameworks. *J. Am. Chem. Soc.* **2016**, *138* (10), 3484–3492.

(8) Chapman, K. W.; Sava, D. F.; Halder, G. J.; Chupas, P. J.; Nenoff, T. M. Trapping Guests within a Nanoporous Metal–Organic Framework through Pressure-Induced Amorphization. *J. Am. Chem. Soc.* **2011**, *133* (46), 18583–18585.

(9) Longley, L.; Collins, S. M.; Zhou, C.; Smales, G. J.; Norman, S. E.; Brownbill, N. J.; Ashling, C. W.; Chater, P. A.; Tovey, R.; Schönlieb, C.-B.; Headen, T.F.; Terrill, N.J.; Yue, Y.; Smith, A.J.; Blanc, F.; Keen, D.A.; Midgley, P.A.; Bennett, T.D. Liquid Phase Blending of Metal-Organic Frameworks. *Nat. Commun.* **2018**, *9* (1), 2135.

(10) Castilho, S.; Borrego, A.; Henriques, C.; Ribeiro, M. F.; Fernandes, A. Monitoring Cobalt Ions Siting in BEA and FER Zeolites by In-Situ UV–Vis Spectroscopy: A DRS Study. *Inorganica Chim. Acta* **2017**, *455*, 568–574.

(11) Trujillano, R.; Villain, F.; Louis, C.; Lambert, J.-F. Chemistry of Silica-Supported Cobalt Catalysts Prepared by Cation Adsorption. 1. Initial Localized Adsorption of Cobalt Precursors. *J. Phys. Chem. C* **2007**, *111* (19), 7152–7164.

(12) Krivanek, O. L.; Lovejoy, T. C.; Dellby, N.; Aoki, T.; Carpenter, R. W.; Rez, P.; Soignard, E.; Zhu, J.; Batson, P. E.; Lagos, M. J.; Egerton, R.F.; Crozier, P.A. Vibrational Spectroscopy in the Electron Microscope. *Nature* **2014**, *514* (7521), 209–212.

(13) Rossouw, D.; Botton, G. A. Plasmonic Response of Bent Silver Nanowires for Nanophotonic Subwavelength Waveguiding. *Phys. Rev. Lett.* **2013**, *110* (6), 066801.

(14) Nicoletti, O.; de la Peña, F.; Leary, R. K.; Holland, D. J.; Ducati, C.; Midgley, P. A. Three-Dimensional Imaging of Localized Surface Plasmon Resonances of Metal Nanoparticles. *Nature* **2013**, *502* (7469), 80–84.

(15) Collins, S. M.; Ringe, E.; Duchamp, M.; Saghi, Z.; Dunin-Borkowski, R. E.; Midgley, P. A. Eigenmode Tomography of Surface Charge Oscillations of Plasmonic Nanoparticles by Electron Energy Loss Spectroscopy. *ACS Photonics* **2015**, *2* (11), 1628–1635.

(16) Nelayah, J.; Kociak, M.; Stéphan, O.; García de Abajo, F. J.; Tencé, M.; Henrard, L.; Taverna, D.; Pastoriza-Santos, I.; Liz-Marzán, L. M.; Colliex, C. Mapping Surface Plasmons on a Single Metallic Nanoparticle. *Nat. Phys.* **2007**, *3* (5), 348–353.

(17) Tizei, L. H. G.; Kociak, M. Spatially Resolved Quantum Nano-Optics of Single Photons Using an Electron Microscope. *Phys. Rev. Lett.* **2013**, *110* (15), 153604.

(18) Alexander, J. A.; Scheltens, F. J.; Drummy, L. F.; Durstock, M. F.; Gilchrist, J. B.; Heutz, S.; McComb, D. W. Measurement of Optical Properties in Organic Photovoltaic Materials Using Monochromated Electron Energy-Loss Spectroscopy. *J. Mater. Chem. A* **2016**, *4* (35), 13636–13645.

(19) Pfannmöller, M.; Heidari, H.; Nanson, L.; Lozman, O. R.; Chrapa, M.; Offermans, T.; Nisato, G.; Bals, S. Quantitative Tomography of Organic Photovoltaic Blends at the Nanoscale. *Nano Lett.* **2015**, *15* (10), 6634–6642.

(20) Herzing, A. A.; Ro, H. W.; Soles, C. L.; DeLongchamp, D. M. Visualization of Phase Evolution in Model Organic Photovoltaic Structures via Energy-Filtered Transmission Electron Microscopy. *ACS Nano* **2013**, *7* (9), 7937–7944.

(21) Gloter, A.; Chu, M.-W.; Kociak, M.; Chen, C. H.; Colliex, C. Probing Non-Dipole Allowed Excitations in Highly Correlated Materials with Nanoscale Resolution. *Ultramicroscopy* **2009**, *109* (11), 1333–1337.

(22) Banerjee, R.; Phan, A.; Wang, B.; Knobler, C.; Furukawa, H.; O'Keeffe, M.; Yaghi, O. M. High-Throughput Synthesis of Zeolitic Imidazolate Frameworks and Application to CO2 Capture. *Science* **2008**, *319* (5865), 939–943.

(23) Tian, Y.-Q.; Chen, Z.-X.; Weng, L.-H.; Guo, H.-B.; Gao, S.; Zhao, D. Y. Two Polymorphs of Cobalt(II) Imidazolate Polymers Synthesized Solvothermally by Using One Organic Template N,N-Dimethylacetamide. *Inorg. Chem.* **2004**, *43* (15), 4631–4635.

(24) Gaillac, R.; Pullumbi, P.; Beyer, K. A.; Chapman, K. W.; Keen, D. A.; Bennett, T. D.; Coudert, F.-X. Liquid Metal–Organic Frameworks. *Nat. Mater.* **2017**, *16* (11), 1149–1154.

(25) de la Peña, F.; Berger, M.-H.; Hochepied, J.-F.; Dynys, F.; Stephan, O.; Walls, M. Mapping Titanium and Tin Oxide Phases Using EELS: An Application of Independent Component Analysis. *Ultramicroscopy* **2011**, *111* (2), 169–176.

(26) Yumashev, K. V.; Denisov, I. A.; Posnov, N. N.; Kuleshov, N. V.; Moncorge, R. Excited State Absorption and Passive Q-Switch Performance of Co2+ Doped Oxide Crystals. *J. Alloys Compd.* **2002**, *341* (1), 366–370.

(27) Ivill, M.; Pearton, S. J.; Rawal, S.; Leu, L.; Sadik, P.; Das, R.; Hebard, A. F.; Chisholm, M.; Budai, J. D.; Norton, D. P. Structure and Magnetism of Cobalt-Doped ZnO Thin Films. *New J. Phys.* **2008**, *10* (6), 065002.

(28) Kresse, G.; Furthmüller, J. Efficiency of Ab-Initio Total Energy Calculations for Metals and Semiconductors Using a Plane-Wave Basis Set. *Comput. Mater. Sci.* **1996**, *6* (1), 15–50.

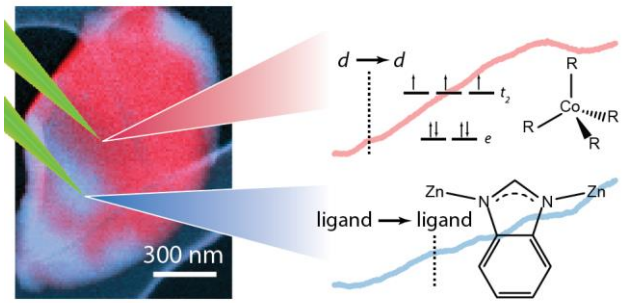
d → d
t2
e
R
Co
R
R
R
Zn
N
N
Zn
ligand → ligand
300 nm